CRYSTAL GROWTH & DESIGN

pubs.acs.org/crystal

Article

Photomechanical Anthracenophane Crystals: Theory, Experiment, and Composite Actuator Performance

Kevin Lam, Pedro Molina-Portillo, Veronica Carta, Tomohiko Nishiuchi, Matthew Ticknor, Ryan C. Hayward, Rabih O. Al-Kaysi, Takashi Kubo, Gregory J. O. Beran,* and Christopher J. Bardeen*

Cite This: *Cryst. Growth Des.* 2025, 25, 8089−8099

Read Online

ACCESS | Metrics & More | Article Recommendations | Supporting Information

ABSTRACT: The anthracene [4 + 4] photocycloaddition is a negative photochromic reaction utilized in photomechanical materials. In crystals, this reaction requires that monomeric anthracene rings adopt a face-to-face packing motif. Anthracenophane derivatives preorganize covalently attached anthracenes for an intramolecular [4 + 4] photocycloaddition reaction, decoupling the photochemistry from the crystal packing. In this work, three anthracenophanes, bi(anthracene-9,10-dimethylene) (**1**), (-H)-monobenzoannulated [2.2](9,10)anthracenophane (**2**) and (-OEt)monobenzoannulated [2.2](9,10)anthracenophane (**3**), are assessed as potential solid-state photomechanical materials. Crystal structures of the reactant and photoproduct forms are obtained, and all crystals exhibit photosalient behavior. Although all three molecules rely on the same photochemistry, theoretical analysis predicts widely varying photomechanical work outputs among these derivatives and their polymorphs, with neat crystals of **2** predicted to exhibit a work density of up to 68 MJ/m^3 due to the favorable alignment of the anthracene ring distortions. Enhanced thermal reversibility is observed for **2** and **3** due to a 60% reduction in the activation energy for photodimer dissociation, leading to recovery of the reactant within minutes at room temperature. The more soluble **3** could be incorporated into a composite ceramic-organic bending actuator that showed good reversibility, although its estimated work density of 2.6×10^3 J/m^3 is several orders of magnitude less than that predicted theoretically for the neat crystal. This large discrepancy suggests that improved processing and actuator design will be required to approach the theoretical limits of these photomechanical crystals.

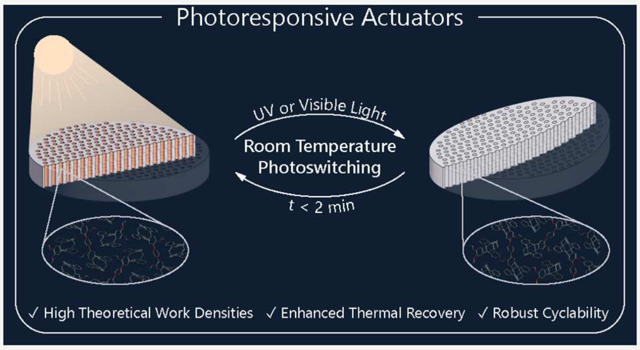

INTRODUCTION

Photochromic molecules have applications across diverse fields, from data storage to superresolution microscopy. The ability to change molecular shape through light absorption can also be harnessed to generate mechanical motion and perform work.[1−4] In all of these applications, the net conversion of reactant to product is determined by penetration of the actinic light through the sample. If the photoisomerization creates a product that also absorbs the excitation light wavelength (positive photochromism), this leads to two interrelated problems. First, it is often the case that the product isomer can photoisomerize back to the reactant form (P-type reversibility). Forward and backward photoisomerization rates eventually equalize to generate a photostationary state (PSS) composed of an equilibrium mixture of reactant and product molecules. Second, the presence of a stable population of absorbers (both reactant and product) limits penetration of the excitation light and prevents conversion of molecules in the interior of optically thick samples.

The twin problems of the PSS and limited optical penetration can be overcome through the use of negative photochromism, in which the photoisomer product absorbs at significantly higher energies, usually as the result of loss of conjugation.[5] Examples of negative photochromic systems include the ring-closing reaction of the donor−acceptor Stenhouse adduct (DASA) family of photochromes,[6−8] as well as [2 + 2] and [4 + 4] photocycloadditions.[9,10] For the latter reaction, anthracene photodimerization is the most commonly used motif,[11,12] either via bimolecular or intramolecular pathways.[13−19] The cyclophane architecture is attractive for efficient [4 + 4] coupling,[20] and Kubo and coworkers recently developed a negative photochromic system based on a pair of anthracenes positioned *ortho* to each other on a phenyl linker.[21−24] The linker positions the anthracenes to undergo facile dimerization while also providing a

Received: June 8, 2025
Revised: August 25, 2025
Accepted: August 26, 2025
Published: September 19, 2025

https://doi.org/10.1021/acs.cgd.5c00851

convenient handle for attaching other functional groups. We recently characterized the photophysical behavior of these anthracenophanes in solution, finding that they support a delocalized charge-transfer state that allows visible light to drive the photodimerization.[25] Furthermore, they undergo photodimerization within 10 ps or less, followed by dimer dissociation over the course of several hours with an activation energy of 94 kJ/mol to regenerate the reactant. The rigidity of the phenyl linker enhances the durability and reversibility of the photochromic reaction.

In molecular crystals, the anthracene [4 + 4] photodimerization reaction has been used to generate photomechanical motion.[26−28] In crystals with head-to-head packing, this photodimerization can be reversed by ambient thermal fluctuations (T-type reversibility), allowing the mechanical motion to be cycled.[29−36] One challenge in these systems has been to identify anthracene derivatives that pack in the correct motif to enable this reversibility. The anthracenophanes build in the head-to-head [4 + 4] reactive geometry, so the crystal packing should not be a determining factor in whether the reaction can proceed. Given this advantage, we wanted to characterize their reactivity in crystal form and assess their potential as solid-state photomechanical materials.

Scheme 1 shows the structures of three representative anthracenophanes: bi(anthracene-9,10-dimethylene) (**1**), (-H)monobenzoannulated [2.2](9,10)anthracenophane (**2**) and (-OEt)monobenzoannulated [2.2](9,10)anthracenophane (**3**). In this paper, we characterize the crystal properties of **2** and **3** and compare them to **1**. Although changing the phenyl substituent from an H atom to an ethoxy (OEt) group has a negligible effect on the solution state properties, we find that the ethoxy substituent leads to crystal polymorphism and solvate formation. Theoretical analysis of all three molecular crystals allows the prediction of different photodimer crystal structures, which are confirmed by experimental results. This analysis suggests that the photomechanical work output is quite different between molecules **1**, **2** and **3**, and that the different crystal forms of **3** have different work outputs as well. The theoretical analysis motivated a deeper study into the solid-state properties of **2** and **3**. The intramolecular [4 + 4] photodimerization was expected to be robust in the solid-state, and we confirmed that all crystal forms exhibit photosalient behavior. More surprisingly, enhanced T-type reversibility arises for **2** and **3**, with a 60% reduction in the activation energy for photodimer dissociation, enabling a recovery of the reactant within minutes at room temperature instead of hours. In order to harness this photomechanical response in a more controlled way, nanowires of **3** were grown in porous ceramic templates. These organic−inorganic composite membranes could generate reversible bending motion. Taken together, there experimental and theoretical results demonstrate that this class of negative photochromes can potentially be used in macroscopic light-driven actuators.

Scheme 1. Chemical Structures of the Compounds Investigated in This Paper: (a) Bi(anthracene-9,10-dimethylene) (1), (-H)mono-benzoannulated [2.2](9,10)anthracenophane (2) and (−OEt)mono-benzoannulated [2.2](9,10)anthracenophane (3). (b) Reaction Scheme Depicting the [4 + 4] Photodimerization Reaction for Molecule 2

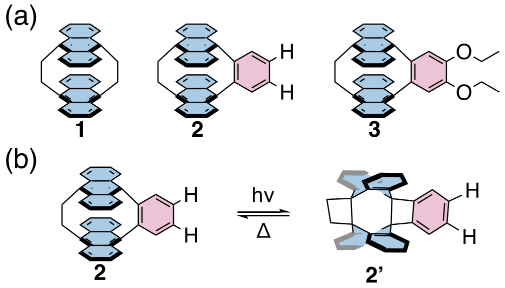

EXPERIMENTAL AND COMPUTATIONAL METHODS

Molecule Synthesis and Bulk Crystal Growth. (-H)-monobenzoannulated [2.2](9,10)anthracenophane (**2**) and (-OEt)-monobenzoannulated [2.2](9,10)anthracenophane (**3**) were synthesized as previously reported.[22] To grow bulk crystals of **2** and **3** suitable for X-ray diffraction analysis, a variety of standard crystallization techniques were employed: **2** (vapor diffusion of *n*-hexane into toluene at 4 °C), **3-NC**/**3-SC** (solvent diffusion of acetone into chloroform at 4 °C), **3-NT** (solvent diffusion of 1-heptanol into toluene at 4 °C), and **3-ST** (slow evaporation of toluene over water at 20 °C). **NC** refers to the neat crystal grown from chloroform, **SC** refers to the solvate crystal grown from chloroform, **NT** refers to the neat crystal grown from toluene, and **ST** refers to the solvate crystal grown from toluene. All samples were kept away from ambient light to prevent formation of the photoisomer.

Preparation of Thin Crystalline Films for UV/vis Spectroscopy Measurements. Approximately 3−5 mg of powder were dissolved in 5 mL of chloroform. Gentle heating (40 °C) and sonication were used to aid in the dissolution of the powder and to back-convert any photoisomer that may have formed during the sample preparation. The resulting solution was then set aside in a dark cabinet. To facilitate the spectroscopy measurements, the thin films were cast inside a standard 1 cm path length quartz cuvette. The quartz cuvette was placed horizontally over a hot plate set to 120 °C and allowed to equilibrate for several minutes. 100 μL of the solution from step 1 was then sequentially injected into the opening of the hot cuvette at a time (1−2 mL total), allowing several seconds in-between for the residual chloroform to evaporate. To confirm the presence of a good optical quality film, UV/vis spectra were periodically collected after every 500 μL of solution was deposited.

Preparation of Organic Filled Anodic Aluminum Oxide Templates. A concentrated solution of (-OEt)monobenzoannulated [2.2](9,10)anthracenophane (**3**) was prepared by adding 2 mg of powder to 70−80 μL of chloroform. The solution was then gently heated (40 °C), sonicated, and subsequently kept in a dark cabinet. Inorganic AAO membrane templates (Whatman, 13 mm diameter, 0.2 μm pore size) were used as received. An empty AAO template was submerged in chloroform to wet the membrane pores and then quickly placed on the surface of a custom-made polytetrafluoroethylene (PTFE) stage. Placed below this PTFE stage was a small piece of Kimwipe (1 × 1 in). Before the AAO template completely dried, the concentrated solution of **3** was quickly deposited on the surface of the membrane. A 150 μL aliquot of chloroform was then rapidly injected onto the small Kimwipe below the stage. Finally, the entire setup was enclosed in an aluminum-covered glass bell jar and allowed to anneal overnight under ambient conditions. To remove the excess material on both sides of the AAO membrane, a series of hand-polishing steps were employed until the surface was smooth. The following sequence of abrasives was used: 9 μm Al_2O_3 → 5 μm SiC → 2 μm Al_2O_3 → 1 μm Al_2O_3 → 0.3 μm Al_2O_3. It is important to note that higher concentrations of **3** did not lead to greater organic loading within the template but rather left excess crystals on top of the template surface.

Composite Actuator Measurements. To measure the deformation of the AAO templates, a modified Michelson interferometer setup was used.[37] AAO templates filled with **3** were placed on top of a

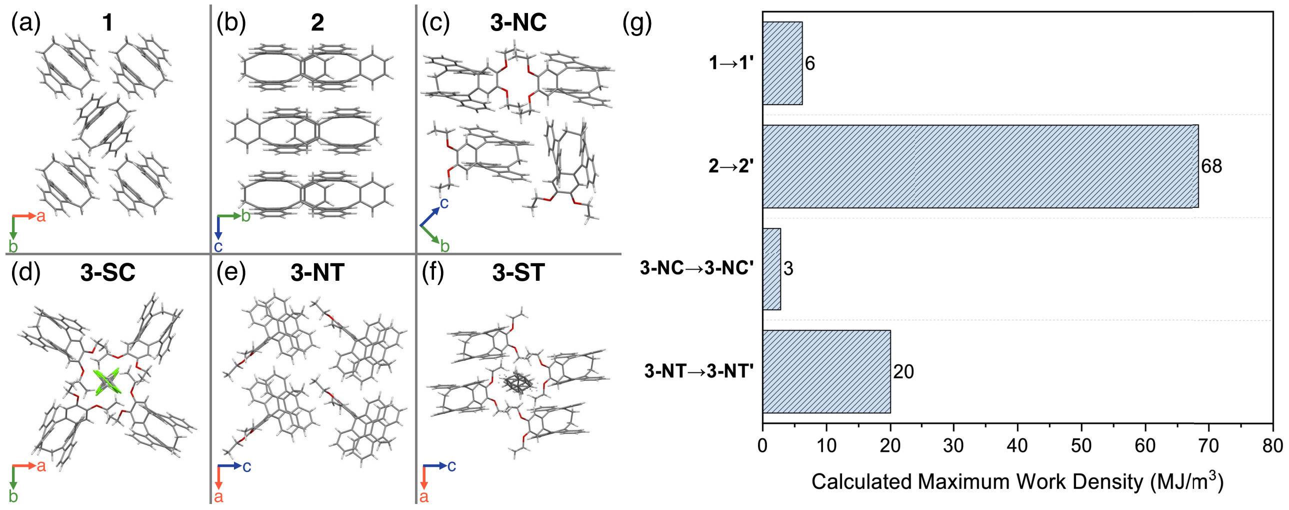

Figure 1. X-ray structures illustrating the varying degrees of parallel alignment of the anthracene rings within the different molecular crystal packings: (a) **1** − neat crystal (CCDC 1103119), (b) **2** − neat crystal (CCDC 1969048), (c) **3-NC** − neat crystal from chloroform (CCDC 2387424), (d) **3-SC** − solvate crystal from chloroform, (e) **3-NT** − neat crystal from toluene, and (f) **3-ST** − solvate crystal from toluene. (g) Calculated maximum work density for the nonsolvate crystal packings, showing that the greatest work is produced for the **2→2′** reaction when adjacent anthracene rings are the most parallel.

1-in. diameter optical flat and then sandwiched in between a half-covered glass microscope slide and a 0.7 g reflective silver mirror. Light from a 632 nm Helium−Neon (0.9 mW) laser was then directed through a beam splitter to act as the probe beam. One of the beams was reflected off a stationary mirror and then projected onto a wall 4.9 m away. The other beam was reflected off the silver mirror and projected to the same wall. The displacement between both beams was used to quantify the extent of bending within the template. To provide the excitation light for these experiments, several different light wavelengths were used: 365 nm (AloneFire SV13 LED flashlight, 29 mW/cm^2), 405 nm (diffused continuous wave laser, 4 mW/cm^2), and 532 nm (diffused continuous wave laser, 6 mW/cm^2).

Optical Spectroscopy Measurements. All samples were prepared in a 1 cm path length quartz cuvette. Steady-state absorption spectra were collected using a Cary 60 UV/vis spectrophotometer. To measure the temperature-dependent recovery kinetics, a Cary 500 UV/vis spectrophotometer with a built-in heating block was used.

Periodic DFT Crystal Structure Optimizations. Periodic DFT structure optimizations began with the experimental crystal structures. Experimental crystal structures of **1** and its photodimer product were obtained from the Cambridge Structure Database (CSD reference codes ANTMEU01 and ANTMET, respectively).[38,39] Experimental crystal structures for the reactant and photodimer products of **2** and **3-NT** obtained here were used for DFT optimizations. For **3-NC**, only the reactant experimental crystal structure was available. Note that the predictions of the photomechanical responses of each species (described below) relied only on the experimental reactant crystal structure as a starting point. Knowledge of the experimental product structures was only used afterward to validate the predicted structure transformations.

Planewave DFT crystal structure optimizations were performed in Quantum Espresso v7.0[40] using the B86bPBE density functional[41,42] paired with the exchange hole dipole moment (XDM) dispersion correction.[43] The calculations employed the projector-augmented wave (PAW) treatment of core electrons, a 50 Ry planewave cutoff, and a Monkhorst−Pack reciprocal space k-point grid with minimum spacing of 0.05 Å^{-1}. Unless otherwise specified, the crystal structure optimizations relaxed both the atomic positions and the lattice parameters.

Since generalized-gradient approximation (GGA) functionals such as B86bPBE-XDM describe the anthracene photodimerization energies poorly,[44,45] the periodic DFT energies were augmented with an intramolecular energy correction computed with spin-component-scaled dispersion-corrected second-order Møller−Plesset perturbation theory (SCS-MP2D).[46] This correction takes the periodic DFT energy of the crystal and adds a correction based on the gas-phase (intramolecular) energy difference between the DFT functional and SCS-MP2D for each molecule i in the unit cell,[47,48]

$$E_{\text{crystal}}^{\text{corrected}} = E_{\text{crystal}}^{\text{DFT}} + \sum_{i=1}^{Z} \left(E_{\text{molec},i}^{\text{SCS-MP2D}} - E_{\text{molec},i}^{\text{DFT}}\right) \tag{1}$$

The gas-phase intramolecular energies were computed using the molecular geometries directly extracted from the DFT-optimized crystal structures. Exploiting the space group symmetry present in these crystals, the gas-phase calculations only need to be performed for the one symmetrically unique molecule per unit cell in practice, and the results are then multiplied by the number of symmetrically equivalent molecules in the unit cell, Z. The intramolecular DFT energies were computed in Quantum Espresso with the same settings as for the crystals, except that the molecule was placed in a large, orthorhombic unit cell with at least 20 Å of vacuum spacing in all directions to mimic the gas phase.[48] The SCS-MP2D gas-phase calculations were performed by using PSI4 v1.5[49] to compute the complete-basis set (CBS) limit MP2 energies and evaluating the spin-component scaling and dispersion correction with the MP2D library.[50] The MP2/CBS energies combine Hartree−Fock/aug-cc-pVQZ with MP2 correlation energies that have been extrapolated to the CBS limit via the two-point extrapolation[51] of energies computed in the aug-cc-pVTZ and aug-cc-pVQZ.

Prediction of Photomechanical Response. The photomechanical response of the crystals was predicted using the topochemical approach developed previously.[52] In this idealized thermodynamic approximation, all molecules in the crystal are assumed to react instantaneously and simultaneously. This approach has successfully predicted solid-state photochemical crystal structure transformations for 9-methyl anthracene, 9-tert-butyl anthracene ester, and several other systems.[52−54] While this paper focuses on the photodimerization reaction of each crystal, the reverse reaction that converts the SSRD back to the monomer can be modeled similarly, and those results are presented in the Supporting Information.

Once the structural transformations have been predicted, idealized anisotropic elastic work densities can be computed. Specifically, the DFT strain (ε) and stress (σ) tensors associated with the deformation from the proto-SSRD to equilibrium SSRD structures are used to calculate the elastic work as a function of crystallographic direction $\hat{n}$,

$$W(\hat{n}) = \frac{-1}{2}\hat{n}^T\sigma\varepsilon\hat{n} \tag{2}$$

The anisotropic work densities are plotted as a heat map projected onto the surface of a sphere to highlight the dependence of the work density on the crystallographic direction.

The idealized assumption that all molecules react instantly and simultaneously should provide an upper bound for the amount of work that can be produced, since it maximizes the stress by changing the molecular shapes faster than the lattice parameters can respond.[52] The work density can exhibit significant path dependence, and we have recently demonstrated that reacting the molecules more slowly can reduce the work density significantly.[55] Here, we focus on the idealized maximum work densities as a straightforward metric for how much work the material might be able to do, while recognizing that there may be challenges in realizing the full predicted work density experimentally.

■ RESULTS AND DISCUSSION

Crystal Structures and Theoretical Photomechanical Work Densities. Crystal structures of all the anthracenophanes in Scheme 1 have been reported previously.[13,22,25,56] We wanted to do a more thorough survey and found that **2** did not exhibit any polymorphism or solvate formation under the growth conditions tested in this work. Derivative **3**, on the other hand, exhibited different polymorphs when grown from $CHCl_3$ and toluene, as well as solvate cocrystals with the same two solvents, for a total of 4 different crystal forms. These are shown in Figure 1 and listed in Table 1 as **3-NC** (neat crystal from $CHCl_3$), **3-SC** (solvate crystal from $CHCl_3$), **3-NT** (neat crystal from toluene), and **3-ST** (solvate crystal from toluene). All crystal forms exhibited photosalient behavior, but we found that visible light from the lamp in the X-ray diffractometer could convert the crystals *in situ* without severe cracking, except for 3-NC. This observation allowed us to obtain the photodimer crystal structure from the same crystal used to obtain the reactant structure. These solid-state reacted dimer (SSRD) crystal structures are denoted **2′**, **3′**, etc. Turoska-Tyrk and co-workers have already characterized the structural transformation of **1**→**1′** in some detail,[56,57] so we used their results in our analysis. The ability to determine the dimerized crystal structures provided a way to define the starting and ending points of the photochemical transformation and experimentally test the DFT topochemical reaction model used to predict photomechanical responses.

Table 1. DFT-Calculated Solid-State Photodimerization Reaction Energies (in kJ/mol) and the Associated Unit Cell Lattice Parameter Changes for 1, 2, 3-NC, and 3-NT

	1 → 1′	2 → 2′	3-NC → 3-NC′	3-NT → 3-NT′
solid-state reaction energies (kJ/mol)	+ 44.9	+ 54.9	+ 68.9	+ 53.8
lattice parameters	**change in unit cell length (%)**			
a	+ 0.4	−4.2	+ 1.4	+ 0.4
b	+ 0.6	+ 0.8	+ 2.2	+ 7.0
c	−2.6	+ 12.7	− 1.5	−5.1
	change in unit cell angle (%)			
α	0.0	0.0	0.0	0.0
β	0.0	+ 3.8	0.0	0.0
γ	0.0	0.0	0.0	0.0

To analyze the work potential for this anthracenophane class of crystals, theoretical calculations were performed on the photodimerization reaction of **1**, **2**, and **3**. Even though **1** is not included in the experimental study, we included it in the theoretical analysis to a obtain broader picture of this class of photomechanical molecular crystals. We began by relaxing experimental crystal structures **1**, **2**, **3-NC**, and **3-NT** monomers with periodic DFT and then predicting the proto-SSRD and equilibrium SSRD for each. For all reactions except **3-NC**, for which the experimental product structure is unknown, the predicted crystal structures of both the reactant and SSRD products overlay well with the experimental ones, with root-mean-square deviation (rmsd15) values ranging 0.1–0.3 Å (Table S8 and Figures S3–S6). These rmsd15 values are consistent with the expected computational errors associated with the DFT model and the neglect of zero-point vibrational energy and thermal expansion. Furthermore, relaxing the experimental product structures with periodic DFT produced structures identical to our predicted SSRDs. The good agreement between the predicted and experimental SSRD structures further validates the computational topochemical approach used to predict the solid-state transformations, adding to the list of successful prediction examples from earlier studies.[52−54]

Table 1 summarizes the computed solid-state photodimerization energies crystal structure lattice parameter changes, and Figure 1g shows the maximum predicted work densities for each reaction. Before discussing the solid-state transformations, we consider how the shape of an isolated anthracenophane molecule changes upon photodimerization. The anthracene rings buckle outward, increasing the carbon–carbon distance between the π-stacked anthracene rings by about 20% at their furthest point. This "butterfly" distortion is accompanied by a smaller (5%) expansion along the short axis of the anthracene rings and a 5% decrease along the long axis. The crystalline photomechanical response reflects the combination of these intramolecular geometry changes and associated changes in the intermolecular separations. The orientations of reactant molecules in the unit cell influence how these molecular-scale changes combine to deform the lattice. For example, if the molecules are all aligned in parallel, one would expect to observe a highly anisotropic structural response, with significant unit cell expansion along the direction of anthracene buckling. When the molecules adopt more varied orientations in the unit cell, however, the net response will likely be smaller and more isotropic. Previous studies of solid-state anthracene photodimerization have found that the largest photomechanical stresses are often produced by the relatively strong forces associated with the anthracene buckling and the steric clashes it generates.[52] The changes in intermolecular spacing along the other directions tend to be energetically "softer" modes that produce less stress.

With these general trends in mind, we now examine the distinct photomechanical responses of the four crystals as predicted by the models. Photodimerization of **1** produces only small changes in the lattice parameters, which is consistent with the varied orientations of the molecules within the unit cell (Figure 1a), and this leads to a small maximum predicted work density of 6 MJ/m^3. The largest lattice parameter change (−2.6%) and highest work density both occur along the *c* axis (Figure 2a), which is largely aligned along the long axis of the anthracene rings. The shortening of the anthracenophane molecules along the long axis upon photodimerization allows the molecules to shift closer together, reducing the *c* lattice parameter. In crystals of **1**, the normally large stress associated

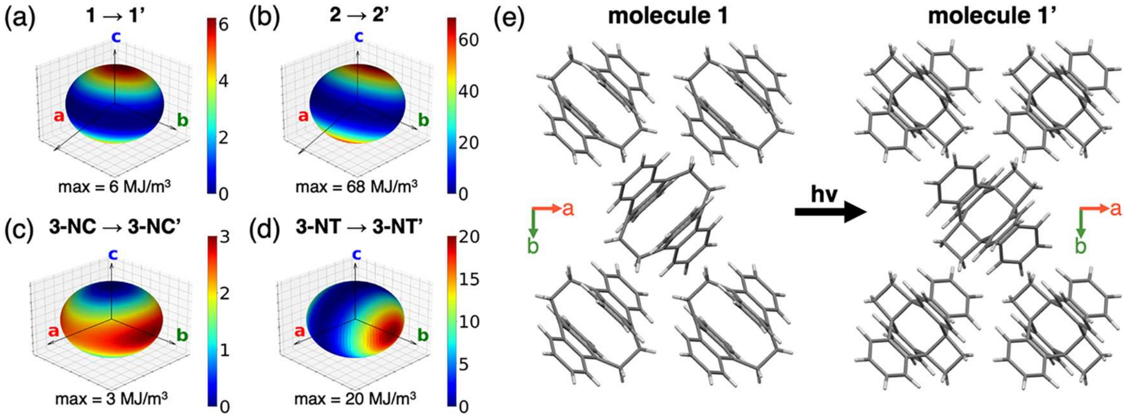

Figure 2. Computationally predicted work density plots showing the anisotropic nature of the mechanical response for the photodimerization reactions of (a) **1**, (b) **2**, (c) **3-NC**, and (d) **3-NT**. The crystallographic axes and the maximum work density for each system are shown. (e) Representative X-ray crystal structures illustrating the geometric changes that occur as molecule **1** undergoes an intramolecular [4 + 4] photodimerization reaction within the crystal.

with the stiff anthracene buckling mode is muted somewhat by how the orientations of the molecules in the cell allow the buckled rings to interdigitate into the spaces between the rings of the neighboring molecules.

3-NC also exhibits varied molecular orientations of the molecules (Figure 1c) that lead to small lattice deformations upon photodimerization, and the transformation again produces a small maximum work density (3 MJ/m^3, Figure 2c). The 1.4% and 2.2% lattice parameter increases along the *a* and *b* axes, respectively, upon photodimerization are associated with the buckling of the anthracene rings causing steric clashes with neighboring molecules. The largest work densities therefore occur in the *ab* plane and reach a maximum along the *b* axis. At the same time, the ring buckling increases the spacing between anthracene rings within the molecule that allows for a small 1.5% compression along the *c* axis.

In contrast to **1** and **3-NC**, the more parallel alignment of **3-NT** molecules in the unit cell (Figure 1e) leads to larger, more anisotropic lattice parameter changes and a considerably larger maximum work density of 20 MJ/m^3 along the *b* direction (Figure 2d). In particular, the distortion caused by the buckling of the anthracene rings has a substantial projection on the *b* axis, which results in a sizable 7.0% predicted expansion of *b*. The greater experimental crystal packing density **3-NT** (1.310 g/cm^3) compared to **3-NC** (1.286 g/cm^3) should also increase the steric clashes upon anthracene ring buckling, effectively increasing the stress generated. In addition to the large expansion along *b*, the molecular shape changes upon photodimerization allow the **3-NT** molecules to shift closer together along *c*, reducing that lattice parameter by 5.1%. However, this mode is much softer than the mode along *b*, and relatively little work density is generated along the *c* axis.

Lastly, **2** exhibits the most favorable crystal packing for generating a large photomechanical response, with the molecules packed in parallel 2-D sheets that leads to a highly anisotropic distortion upon photodimerization. The model predicts a 12.7% lattice parameter expansion along the *c* axis, which is associated with the anthracene buckling direction. This is the largest deformation seen for any of these four systems, and **2** is predicted to have the correspondingly largest associated maximum work density of 68 MJ/m^3 (Figure 2b). Once again, the shortening of the molecule along the long anthracene ring axis enables the crystal to shrink −4.2% along the *a* axis, though this softer mode produces comparatively little work density.

In summary, the maximum predicted work densities for the bis(anthrancene) derivatives follow the trend **2** > **3-NT** > **1** ≈ **3-NC** and are closely related to the anisotropy of the crystal structure transformation. The largest stresses and strains are associated with the buckling of the anthracene rings, and molecular packing that concentrates these distortions along a single axis maximizes the photomechanical response. The contrast in reaction energetics, structural deformations, and work densities between **3-NC** and **3-NT** highlight the importance of polymorphism, similar to what was found for polymorphic diarylethenes[53] and cinnamalonitrile[58] derivatives.

Finally, we examine the reaction energetics for all four crystals. The solid-state photodimerization of **1** is endothermic at 39 kJ/mol, and the reaction energy increases to 57 kJ/mol for **3-NT**, 69 kJ/mol for **2**, and 82 kJ/mol for **3-NC**. The increased endothermicity of the latter three crystals highlights how the bridging phenyl strains the photodimer product. Computing the gas reaction energies on the molecular geometries extracted directly from the crystal (i.e., without relaxing the molecular geometries in the gas phase), we find that the **1** and **3-NT** gas-phase reaction energies are within 4−6 kJ/mol of the crystalline one, suggesting the crystalline environment has a fairly weak influence on the reaction energy. On the other hand, the crystalline environment increases the reaction energy for **2** and **3-NC** by a more sizable 14−15 kJ/mol. We also observe that the maximum carbon−carbon distance in **3-NC** increases only 16% upon photodimerization, compared to 23% in **3-NT**. Together, these results suggest that the crystal packing in **3-NC** hinders anthracene buckling more than in **3-NT**, and it highlights the importance of crystal packing and polymorphism.

Spectroscopy and Reaction Dynamics. The theoretical results in the previous Section suggest that the anthracenophane crystals could function as photomechanical materials. In order to further analyze their potential for this application, we needed to assess their light absorption properties. The intramolecular anthracene ring separation in all the crystal structures is significantly less than any intermolecular separation, so we expect intermolecular exciton formation to be negligible. Representative absorption spectra of thin

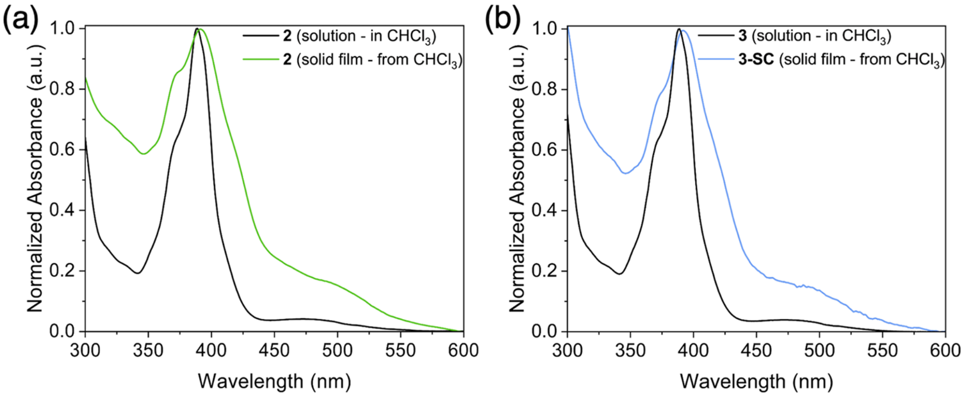

Figure 3. Normalized steady-state UV/vis absorption spectra of (a) **2** and (b) **3**, both prepared as a dilute solution (30 μM) in $CHCl_3$ and as a thin polycrystalline film.

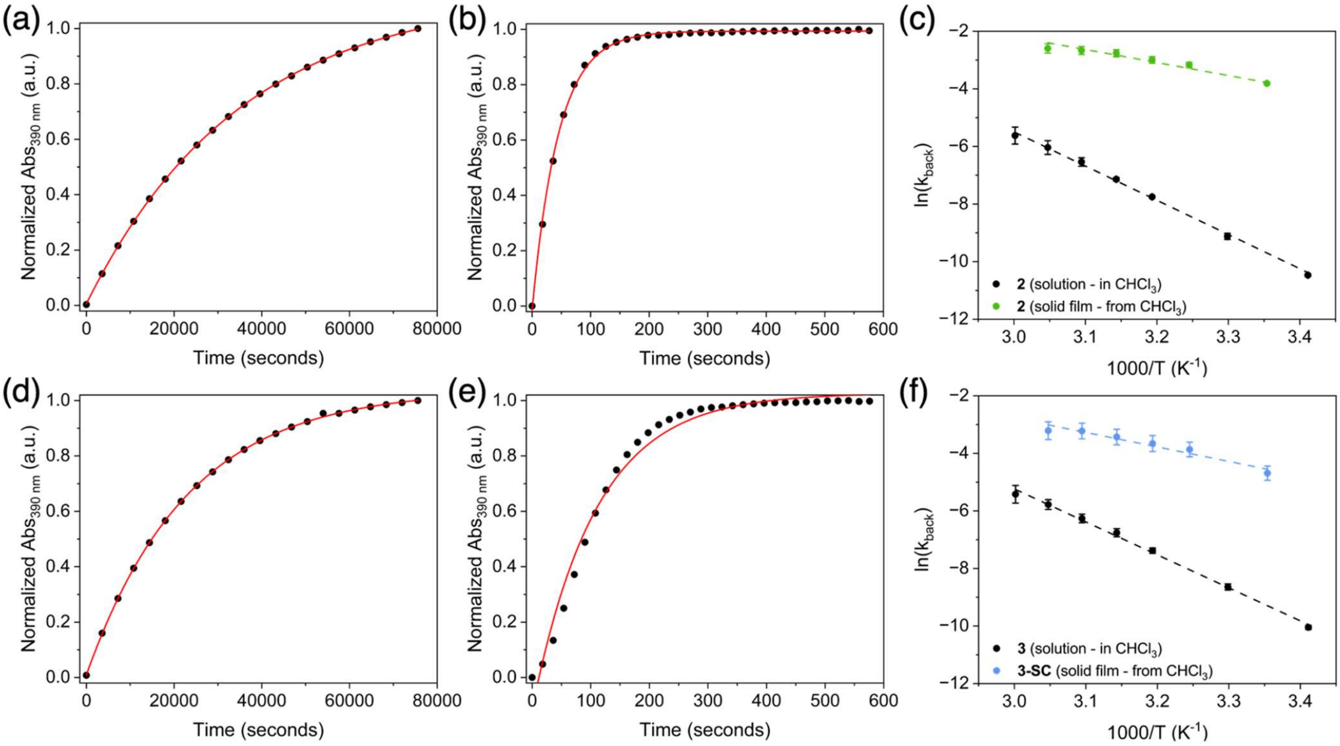

Figure 4. Thermal recovery kinetics of (a) **2** in $CHCl_3$ at 20 °C and (b) **2** as a thin film at 25 °C, both measured over time via UV/vis spectroscopy. (c) Arrhenius plots for the thermal recovery process of **2** in solution and as a solid, showing that the recovery kinetics are several orders of magnitude faster in the solid phase. Thermal recovery kinetics of (d) **3** in $CHCl_3$ at 20 °C and (e) **3-SC** as a thin film at 25 °C. (f) Arrhenius plots for the thermal recovery process of **3** in solution and as a solid, showing similar recovery trends to **2**. Experimentally determined activation energy barriers (E_a) and Arrhenius prefactors (A): $\mathbf{2}_{\mathbf{solution}}$ ($E_a = 98.8 \pm 3.0$ kJ/mol | A = 1×10^{13} s^{-1}) $\mathbf{2}_{\mathbf{solid}}$ ($E_a = 37.6 \pm 3.0$ kJ mol^{-1} | A = 9×10^{4} s^{-1}) $\mathbf{3}_{\mathbf{solution}}$ ($E_a = 95.3$ kJ $\pm$ 2.6 kJ/mol | A = 5×10^{12} s^{-1}) $\mathbf{3\text{-}SC}_{\mathbf{solid}}$ ($E_a = 41.9 \pm 4.9$ kJ/mol | A = 2×10^{5} s^{-1}).

polycrystalline films of **2** and **3-SC** shown in Figures 3a,b closely resemble those of the isolated molecules in solution, as expected. Notable differences include increased broadening and a peak redshift of ∼ 5 nm in the solid-state spectra. Both effects are commonly seen due to the higher dielectric constant of the solid.[59] The most important change in the absorption line shape is the enhanced oscillator strength of the S_A charge-transfer resonance state peaked at around 500 nm. This feature results from the intramolecular interaction between the anthracene pair, while the neutral excited state localized on one anthracene (S_B) gives rise to the absorption peaked around 390 nm. In solution, the S_A band is about 5% of the localized S_B state intensity, but in the solid it rises to about 20% of the S_B intensity. Since the S_A state also has a higher quantum yield for photodimerization,[25,60] this enhancement should facilitate conversion by visible light in the crystal, providing an alternative to the ultraviolet light usually required to initiate the anthracene [4 + 4] photodimerization. Indeed, we observed that all crystals underwent rapid photodimerization, as judged by their loss of color under UV and visible light exposure.

Useful actuator performance depends on the thermal (T-type) reversibility of the photochemical reaction. In general, a faster reset time is preferred. In solution, the rigid phenyl linker destabilizes the cyclobutene rings formed upon photodimerization and shortens the T-type recovery time from

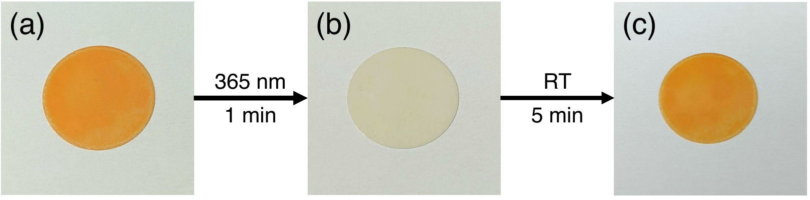

Figure 5. Photographic images showing the negative photochromism and subsequent recovery of a light-responsive anodic aluminum oxide (AAO) template filled with **3-NC**/**3-SC** nanorods: (a) before photolysis, (b) after photolysis at 365 nm for 1 min, and (c) full recovery after 5 min under ambient conditions (25 °C).

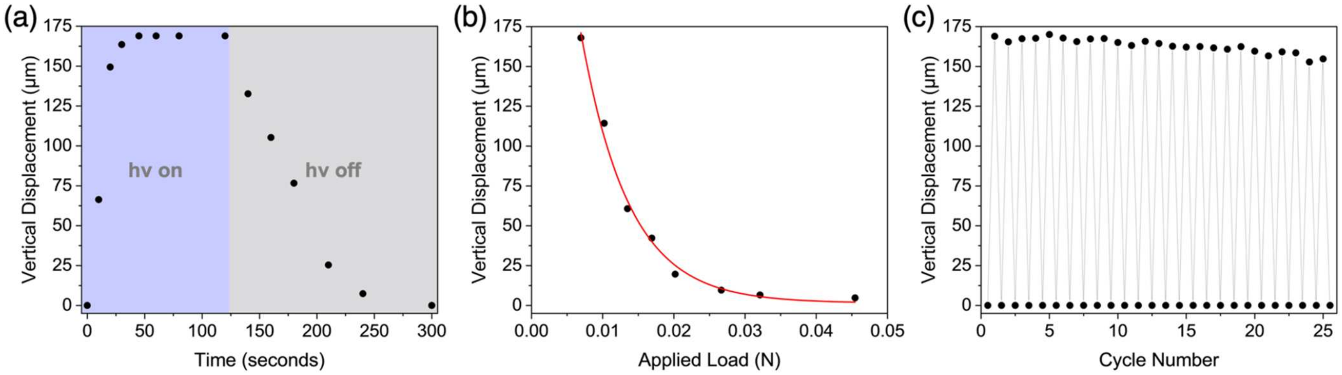

Figure 6. Experimental actuator performance of an anodic aluminum oxide template filled with **3-NC**/**3-SC** nanorods. (a) Vertical template displacement as a function of 365 nm irradiation time (29 mW/cm^2), showing full conversion within 1 min of photolysis and the subsequent template recovery within 2 min under ambient conditions. (b) Vertical template displacement as a function of variable applied load, shown with a single exponential fit and a calculated work density of 2.6 × 10^3 J/m^3. (c) Vertical template displacement under 25 repeated cycles of photolysis at 365 nm for 1 min, followed by ambient recovery for 5 min.

days for **1** to hours for **2** and **3**.[25] But when **2** and **3** are reacted in their crystal forms, the recovery time is shortened to only a few minutes. Figures 4a,b compare the anthracene absorption recovery dynamics of **2** in solution and in the crystal, showing a factor of 100 rate increase for the crystal form. **3** and **3-SC** were also examined and show a similar rapid acceleration of the photodimer dissociation in the crystal form (Figures 4d,e).

The 100× faster dimer dissociation in the crystals was surprising. Previous work has shown that the rate of thermal dissociation is sensitive to both molecular structure[61] and local mechanical pressure.[62] It is likely that the photodimer is subject to additional strain due to the constraints of the crystal environment. To examine the physical origin of the rate enhancement in more detail, we performed temperature-dependent rate measurements on polycrystalline films of **2** and **3-SC**. Over the temperature range 20−60 °C, exponential fits to the absorption recovery yielded rates that could be used to make an Arrhenius plot. Arrhenius plots of the solution and crystal rate data are compared in Figures 4c,f. For **2**, the activation energy E_{act} = 37.6 ± 3.0 kJ/mol is about 40% of that measured in solution.[25] The prefactor $A = 9 \times 10^4$ s^{-1} is much lower than that of the solution reaction, which prevents an even more dramatic decrease in the recovery time. Similarly, the activation energy and prefactor for **3-SC** are E_{act} = 41.9 ± 4.9 kJ/mol and $A = 2 \times 10^5$ s^{-1} respectively. It is possible that packing constraints in the crystal environment prepositions the dimer closer to its transition state, lowering and/or lessening the need for conformational distortions needed for dissociation. The origin of the low A values is less clear. One possibility is that the rigid crystal environment decreases the frequency of reactive events leading to dissociation. However, it may also indicate that the dissociation reaction is not a simple one-step process. Deviations from linearity in the solution Arrhenius plots also indicated that the dissociation may require multiple steps.[63,64]

Composite Membrane Actuator Performance. All crystals containing **1**-**3** exhibited photosalient behavior (Figure S7), but the favorable reversibility and potential work densities of the **2** and **3** crystals motivated us to examine whether they could form the basis of photomechanical actuators. We used our previously developed strategy of growing crystalline nanowires inside porous anodic aluminum oxide (AAO) templates by solvent infiltration and annealing. The low solubility of **2** prevented us from successfully growing it inside the templates, but we were able to grow nanowires inside the AAO using a concentrated **3**/$CHCl_3$ solution. By weighing the AAO template before and after filling, we estimated that 0.6 mg of **3** could be deposited. Assuming an organic density of 1.26 g/cm^3 and a 50% porosity of the template,[65] this mass of **3** corresponds to a filling fraction of ∼12% of the available void space. The filled template exhibited the same reversible photochromic behavior as the neat crystals (Figure 5). X-ray diffraction experiments showed that both **3-NC** and **3-SC** crystal peaks were present (Figures S10−S11), which was not unexpected since both forms could be easily grown from $CHCl_3$ solutions.

When one-half of a filled template was irradiated from the bottom, it would bend up and tilt a 0.7 g mirror placed on top of it. The mechanical performance of this bending actuator was characterized using standard optical lever methods.[37] Figure 6 summarizes the performance of this photomechanical membrane actuator. When exposed to 365 nm light (29 mW cm^{-2}) the bending reached a maximum displacement of 175 μm within 50 s. While the light was left on, the bend could be maintained indefinitely, but after it was turned off, the membrane relaxed to its original flat shape within 120 s

(Figure 6a). Reversible actuation was also observed using 405 and 532 nm light (Figure S12). The relaxation after illumination was too slow for thermal heat loss but matched the photodimer dissociation rate measured by optical absorption in thin films of **3-SC**. By varying the mass on top of the template, the work displacement curve in Figure 6b could be measured. The effective stopping force for this actuator was ∼ 0.05 N, about 10× less than for bending actuators that used a diarylethene (DAE) derivative as the active material.[37] Integration of the force−displacement curve in Figure 6b yielded the work output of 1.2×10^{-6} J. When this output was divided by the volume of organic inside the template, we obtained an estimate of the volumetric work density of 2.6×10^3 J/m^3, comparable to that observed for the DAE composites[37,66] (Table S9) and for single bending crystals.[67] The mirror displacement could be repeated for multiple cycles, confirming the reversibility of the actuator, but a slow decrease in performance was observed over 25 cycles (Figure 6c). When the template had to lift higher loads, a more rapid loss of reversibility was observed. Given the high stability of **3** in solution,[25] we suspect that the loss of lifting capacity likely results from crystal fracture within the template that randomizes the alignment and fills some of the available void space.

It was surprising that even under conditions of high intensity radiation, the template composite still showed bending. Bending usually requires a gradient across the thickness of the template. A negative photochrome should enable complete conversion to product across the entire thickness. However, the distribution of crystals inside the template is determined by the ability of the growth solvent to uniformly infiltrate the pores. Forces due to gravity and evaporation could make the solvent penetration (and crystal growth) less homogeneous. Similarly, surface polishing can introduce an anisotropy due to uneven disruption of crystals embedded in one surface. Both sources of heterogeneity could cause bending even after complete conversion to photoproduct.[66]

It was somewhat disappointing that the measured work density of **3** in the AAO template was several orders of magnitude less than that calculated for the photoinduced expansion of **3-NC**. There are multiple reasons that could explain this shortfall. First, the crystals in the template are a mixture of **3-NC** and **3-SC**, and the solvate crystal **3-SC** is expected to have a lower work density than the neat crystal, if only because it has a lower density of active units. Second, the orientation of the crystals within the template channels may not be ideal for transmitting work to the walls to drive bending. For example, if the *c* axis is aligned with the channel, most of the crystal work is directed along the channel and does not push against the walls to induce bending. Third, the AAO template material is not ideal for actuation. The elastic modulus of Al_2O_3 is much higher than that of the organic component, which leads to a mechanical impedance mismatch as the softer organic tries to deform the harder ceramic.[68] Fourth, the bending mode of actuation is less effective than expansion, usually by an order of magnitude, which also reduces the total work output. Fifth, almost 90% of the space available inside the template does not contain active material. This void space provides a sort of pressure relief valve for the photoinduced crystal expansion that allows it to bypass applying pressure to the sides of the channel. Finally, the work is path dependent, and the work produced when the molecules react more slowly may be less than that from a fully concerted crystalline reaction.[55]

CONCLUSIONS

This paper has presented a combined experiment and theory approach to assess the potential of a new class of anthracenophanes as solid-state photomechanical materials. They provide a new material platform for solid-state photomechanical actuators with some advantages relative to the DAEs used in our previous work.[37,66,69,70] First, they are T-type photochromes that reset by themselves, at room temperature, without the need for a second light exposure. Second, their absorption extends into the visible wavelength range. Third, they are negative photochromes that enable 100% conversion of the sample, regardless of thickness. The intramolecular [4 + 4] photodimerization reaction is insensitive to crystal packing, unlike monomeric anthracene derivatives. The photodimer dissociation occurs 100× more rapidly in the crystalline state, leading to enhanced reversibility. Enhanced absorption strength of the CT feature around 500 nm allows the photochemistry to be more easily driven by visible light. Crystal structures of the reactant and photoproduct forms support theoretical predictions that **2** can generate a work density of up to 68 MJ/m^3. The more soluble **3** was incorporated into a composite ceramic-organic bending actuator that showed good reversibility, although its estimated work density of 2.6×10^3 J/m^3 is several orders of magnitude less than predicted theoretically. This large discrepancy suggests that improved processing and actuator design will be required to approach the theoretical work output limits of these promising photomechanical crystals.

ASSOCIATED CONTENT

Supporting Information

The Supporting Information is available free of charge at https://pubs.acs.org/doi/10.1021/acs.cgd.5c00851.

Crystal data and structure refinement for **2′**, **3-SC**, **3-SC′**, **3-NT**, **3-NT′**, **3-ST**, and **3-ST′**; maximum work densities; anisotropic work density plots; RMSD15 comparison between experimental and theoretical structures; crystal structure overlay for **1** and **1′**, **2** and **2′**, **3-NC**, **3-NT**, and **3-NT′**; optical microscopy images of all crystals; electron microscopy images of **3-NT**; electron microscopy image of **3-NC**/**3-SC**; powder XRD of **3**, X-ray scattering of **3** nanorods; actuator performance of **3-NC**/**3-SC** nanorods; crystal work density calculation (PDF)

Accession Codes

Deposition Numbers 2445884−2445890 contain the supplementary crystallographic data for this paper. These data can be obtained free of charge via the joint Cambridge Crystallographic Data Centre (CCDC) and Fachinformationszentrum Karlsruhe Access Structures service.

AUTHOR INFORMATION

Corresponding Authors

Gregory J. O. Beran − *Department of Chemistry, University of California, Riverside, Riverside, California 92521, United States*; orcid.org/0000-0002-2229-2580;
Email: gregory.beran@ucr.edu
Christopher J. Bardeen − *Department of Chemistry, University of California, Riverside, Riverside, California*

92521, United States; orcid.org/0000-0002-5755-9476; Email: christopher.bardeen@ucr.edu

Authors

Kevin Lam – *Department of Chemistry, University of California, Riverside, Riverside, California 92521, United States;* orcid.org/0009-0007-6606-8170

Pedro Molina-Portillo – *Department of Chemistry, University of California, Riverside, Riverside, California 92521, United States*

Veronica Carta – *Department of Chemistry, University of California, Riverside, Riverside, California 92521, United States;* orcid.org/0000-0001-8089-8436

Tomohiko Nishiuchi – *Department of Chemistry, Graduate, School of Science, Osaka University, 560-0043 Osaka, Japan;* orcid.org/0000-0002-2113-0731

Matthew Ticknor – *Materials Science and Engineering, University of Colorado Boulder, Boulder, Colorado 80303, United States*

Ryan C. Hayward – *Materials Science and Engineering, University of Colorado Boulder, Boulder, Colorado 80303, United States; Department of Chemical and Biological Engineering, University of Colorado Boulder, Boulder, Colorado 80303, United States;* orcid.org/0000-0001-6483-2234

Rabih O. Al-Kaysi – *College of Science and Health Professions-3124, King Saud bin Abdulaziz University for Health Sciences, and King Abdullah International Medical Research Center (Nanomedicine), Ministry of National Guard Health Affairs, Riyadh 11426, Kingdom of Saudi Arabia;* orcid.org/0000-0001-8429-2802

Takashi Kubo – *Department of Chemistry, Graduate, School of Science, Osaka University, 560-0043 Osaka, Japan;* orcid.org/0000-0001-6809-7396

Complete contact information is available at: https://pubs.acs.org/10.1021/acs.cgd.5c00851

Notes

The authors declare no competing financial interest.

■ ACKNOWLEDGMENTS

This work was supported by ONR under grant/contract N00014-24-1-2358 (C.J.B., R.C.H., and G.J.O.B). The views expressed are those of the author and do not reflect the official policy or position of the Department of Defense or the U.S. Government. This work was also supported by the King Abdullah International Medical Research Center (KSAU-HS/KAIMRC) through grant NRC21R25003 (R.O.A.-K.) and by JSPS KAKENHI Grant-in-Aid for Scientific Research (C) JP20K05475 (T.N.) and Scientific Research (B) 24K01454 (T.N.). G.J.O.B gratefully acknowledges supercomputer time from ACCESS (CHE110064) and the computer clusters and data storage resources of the U.C. Riverside High-Performance Computing Center, which were funded by grants from NSF (MRI-2215705, MRI-1429826) and NIH (1S10OD016290-01A1).

■ REFERENCES

(1) Irie, M.; Yokoyama, Y.; Seki, T. *New Frontiers in Photochromism*; Springer: Tokyo, 2013.

(2) Kim, T.; Zhu, L.; Al-Kaysi, R. O.; Bardeen, C. J. Organic photomechanical materials. *ChemPhysChem* **2014**, *15*, 400–414.

(3) Naumov, P.; Chizhik, S.; Panda, M. K.; Nath, N. K.; Boldyreva, E. Mechanically Responsive Molecular Crystals. *Chem. Rev.* **2015**, *115*, 12440–12490.

(4) White, T. J. *Photomechanical Materials, Composites, and Systems*, 1st ed.; Wiley: Hoboken, NJ, 2017.

(5) Aiken, S.; Edgar, R. J. L.; Gabbutt, C. D.; Heron, B. M.; Hobson, P. A. Negatively Photochromic Organic Compounds: Exploring the Dark Side. *Dyes Pigm.* **2018**, *149*, 92–121.

(6) Helmy, S.; Oh, S.; Leibfarth, F. A.; Hawker, C. J.; Alaniz, J. R. d. Design and Synthesis of Donor–Acceptor Stenhouse Adducts: A Visible Light Photoswitch Derived from Furfural. *J. Org. Chem.* **2014**, *79*, 11316–11329.

(7) Zulfikri, H.; Koenis, M. A. J.; Lerch, M. M.; Donato, M. D.; Szymański, W.; Filippi, C.; Feringa, B. L.; Buma, W. J. Taming the Complexity of Donor–Acceptor Stenhouse Adducts: Infrared Motion Pictures of the Complete Switching Pathway. *J. Am. Chem. Soc.* **2019**, *141*, 7376–7384.

(8) Clerc, M.; Sandlass, S.; Rifaie-Graham, O.; Peterson, J. A.; Bruns, N.; Alaniz, J. R. d.; Boesel, L. F. Visible light-responsive materials: the (photo)chemistry and applications of donor–acceptor Stenhouse adducts in polymer science. *Chem. Soc. Rev.* **2023**, *52*, 8245–8294.

(9) Tomlinson, W. J.; Chandross, E. A.; Fork, R. L.; Pryde, C. A.; Lamola, A. A. Reversible Photodimerization: a New Type of Photochromism. *Appl. Opt.* **1972**, *11*, 533–548.

(10) Dürr, H.; Bouas-Laurent, H. *Photochromism: Molecules and Systems*, 1st ed.; Elsevier Science: Amsterdam, Netherlands, 2003.

(11) Bouas-Laurent, H.; Castellan, A.; Desvergne, J.-P.; Lapouyade, R. Photodimerization of anthracenes in fluid solution: structural aspects. *Chem. Soc. Rev.* **2000**, *29*, 43–55.

(12) Bouas-Laurent, H.; Castellan, A.; Desvergne, J.-P.; Lapouyade, R. Photodimerization of anthracenes in fluid solutions: (part 2) mechanistic aspects of the photocycloaddition and of the photochemical and thermal cleavage. *Chem. Soc. Rev.* **2001**, *30*, 248–263.

(13) Golden, J. H. Bi(anthracene-9,10-dimethylene)(tetrabenzo-[2,2]-paracyclophane]. *J. Chem. Soc.* **1961**, 3741–3748.

(14) De Schryver, F. C.; Boens, N.; Huybrechts, J.; Daemen, J.; Brackelaire, M. D. Photochemistry of bichromophoric compounds: scope and expectations. *Pure Appl. Chem.* **1977**, *49*, 237–247.

(15) Bergmark, W. R.; II, G. J.; Reinhardt, T. E.; Halpern, A. M. Photoisomerization of bis(9-anthryl)methane and other linked anthracenes. The role of excimers and biradicals in photodimerization. *J. Am. Chem. Soc.* **1978**, *100*, 6665–6673.

(16) Yamashita, I.; Fujii, M.; Kaneda, T.; Misumi, S.; Otsubo, T. Synthetic macrocyclic ligands. II. Synthesis of a photochromic crown ether. *Tetrahedron Lett.* **1980**, *21*, 541–544.

(17) Desvergne, J.-P.; Fages, F.; Bouas-Laurent, H.; Marsau, P. Tunable photoresponsive supramolecular systems. *Pure Appl. Chem.* **1992**, *64*, 1231–1238.

(18) Rettig, W.; Paeplow, B.; Herbst, H.; Müllen, K.; Desvergne, J.-P.; Bouas-Laurent, H. Intramolecular excimer formation in short- and long-chainlength di(9-anthryl) bichromophoric compounds and relation to ground state properties. *New J. Chem.* **1999**, *23*, 453–460.

(19) Liang, C.-K.; Desvergne, J.-P.; Bassani, D. M. Anthracene photodimerization in a bis-chromophoric hydrogen-bonding receptor. *Photochem. Photobiol. Sci.* **2014**, *13*, 316–323.

(20) Oguma, Y.; Yamamoto, M.; Sunatsuki, Y.; Ota, H.; Yamaji, M.; Okamoto, H. Intramolecular [π4s + π4s] photocycloaddition of carbon- and nitrogen-bridged [3_2](1,4)naphthalenophanes. *Photochem. Photobiol. Sci.* **2024**, *23*, 1509–1519.

(21) Nishiuchi, T.; Uno, S.-y.; Hirao, Y.; Kubo, T. Intramolecular Interaction, Photoisomerization, and Mechanical C–C Bond Dissociation of 1,2-Di(9-anthryl)benzene and Its Photoisomer: A Fundamental Moiety of Anthracene-Based π-Cluster Molecules. *J. Org. Chem.* **2016**, *81*, 2106–2112.

(22) Nishiuchi, T.; Kisaka, K.; Kubo, T. Synthesis of Anthracene-Based Cyclic p-Clusters and Elucidation of their Properties Originating from Congested Aromatic Planes. *Angew. Chem., Int. Ed.* **2021**, *60*, 5400–5406.

(23) Nishiuchi, T.; Makihara, Y.; Kishi, R.; Sato, H.; Kubo, T. Stacked antiaromaticity in the π-congested space between the aromatic rings in the anthracene dimer. *J. Phys. Org. Chem.* **2023**, *36*, No. e4451.

(24) Nishiuchi, T.; Takeuchi, S.; Makihara, Y.; Kimura, R.; Saito, S.; Sato, H.; Kubo, T. Synthesis, Properties, and Intermolecular Interactions in the Solid States of π-Congested X-Shaped 1,2,4,5-Tetra(9-anthryl)benzenes. *Bull. Chem. Soc. Jpn.* **2022**, *95*, 1591−1599.

(25) Lam, K.; Dillon, R. J.; Carreras, A.; Nishiuchi, T.; Kubo, T.; Al-Kaysi, R. O.; Casanova, D.; Bardeen, C. J. Using an aromatic linker to optimize charge-resonance states, photodimerization and reversibility in covalent anthracene dimers. *Phys. Chem. Chem. Phys.* **2025**, *27*, 5305−5316.

(26) Al-Kaysi, R. O.; Muller, A. M.; Bardeen, C. J. Photochemically driven shape changes of crystalline organic nanorods. *J. Am. Chem. Soc.* **2006**, *128*, 15938−15939.

(27) Tong, F.; Bardeen, C. J.; Al-Kaysi, R. O. Photomechanical Crystals Made from Anthracene Derivatives. In *Mechanically Responsive Materials for Soft Robotics*; Koshima, H., Ed.; Wiley, 2020.

(28) Salzillo, T.; Brillante, A. Commenting on the Photoreactions of Anthracene Derivatives in the Solid State. *CrystEngComm* **2019**, *21*, 3127−3136.

(29) Ito, Y.; Fujita, H. Formation of an unstable photodimer from 9-anthracenecarboxylic acid in the solid state. *J. Org. Chem.* **1996**, *61*, 5677−5680.

(30) Al-Kaysi, R. O.; Bardeen, C. J. Reversible photoinduced shape changes of crystalline organic nanorods. *Adv. Mater.* **2007**, *19*, 1276−1280.

(31) Good, J. T.; Burdett, J. J.; Bardeen, C. J. Using two-photon excitation to control bending motions in molecular-crystal nanorods. *Small* **2009**, *5*, 2902−2909.

(32) Zhu, L.; Al-Kaysi, R. O.; Bardeen, C. J. Reversible photo-induced twisting of molecular crystal microribbons. *J. Am. Chem. Soc.* **2011**, *133*, 12569−12575.

(33) Zhu, L.; Al-Kaysi, R. O.; Bardeen, C. J. Photoinduced Ratchet-Like Rotational Motion of Branched Molecular Crystals. *Angew. Chem., Int. Ed.* **2016**, *55*, 7073−7076.

(34) Zhu, L.; Al-Kaysi, R. O.; Dillon, R. J.; Tham, F. S.; Bardeen, C. J. Crystal structures and photophysical properties of 9-anthracene carboxylic acid derivatives for photomechanical applications. *Cryst. Growth Des.* **2011**, *11*, 4975−4983.

(35) Zhu, L.; Tong, F.; Salinas, C.; Al-Muhanna, M. K.; Tham, F. S.; Kisailus, D.; Al-Kaysi, R. O.; Bardeen, C. J. Improved Solid-State Photomechanical Materials by Fluorine Substitution of 9-Anthracene Carboxylic Acid. *Chem. Mater.* **2014**, *26*, 6007−6015.

(36) Salzillo, T.; Venuti, E.; Femoni, C.; Valle, R. G. D.; Tarroni, R.; Brillante, A. Crystal Structure of the 9-Anthracene−Carboxylic Acid Photochemical Dimer and Its Solvates by X-ray Diffraction and Raman Microscopy. *Cryst. Growth Des.* **2017**, *17*, 3361−3370.

(37) Dong, X.; Tong, F.; Hanson, K. M.; Al-Kaysi, R. O.; Kitagawa, D.; Kobatake, S.; Bardeen, C. J. Hybrid Organic-Inorganic Photon Powered Actuators Based on Aligned Diarylethene Nanocrystals. *Chem. Mater.* **2019**, *31*, 1016−1022.

(38) Harada, J.; Ogawa, K.; Tomoda, S. The Central C−C Bond Length in the Bi(anthracene-9,10-dimethylene) Photoisomer: Unusual Elongation and Crystalline State Reaction. *Chem. Lett.* **1995**, *24*, 751−752.

(39) Ehrenberg, M. The crystal structure of bi(anthracene-9,10-dimethylene photo-isomer). *Acta Crystallogr.* **1966**, *20*, 182−186.

(40) Giannozzi, P.; Andreussi, O.; Brumme, T.; Bunau, O.; Nardelli, M. B.; Calandra, M.; Car, R.; Cavazzoni, C.; Ceresoli, D.; Cococcioni, M.; Colonna, N.; Carnimeo, I.; Corso, A. D.; Gironcoli, Sd.; Delugas, P.; Jr, R. A. D.; Ferretti, A.; Floris, A.; Fratesi, G.; Fugallo, G.; Gebauer, R.; Gerstmann, U.; Giustino, F.; Gorni, T.; Jia, J.; Kawamura, M.; Ko, H.-Y.; Kokalj, A.; Küçükbenli, E.; Lazzeri, M.; Marsili, M.; Marzari, N.; Mauri, F.; Nguyen, N. L.; Nguyen, H.-V.; Otero-de-la-Roza, A.; Paulatto, L.; Poncé, S.; Rocca, D.; Sabatini, R.; Santra, B.; Schlipf, M.; Seitsonen, A. P.; Smogunov, A.; Timrov, I.; Thonhauser, T.; Umari, P.; Vast, N.; Wu, X.; Baroni, S. Advanced capabilities for materials modelling with Quantum ESPRESSO. *J. Phys.: Condens. Matter* **2017**, *29*, No. 465901.

(41) Becke, A. D. On the large-gradient behavior of the density functional exchange energy. *J. Chem. Phys.* **1986**, *85*, 7184−7187.

(42) Perdew, J. P.; Burke, K.; Ernzerhof, M. Generalized Gradient Approximation Made Simple. *Phys. Rev. Lett.* **1996**, *77*, 3865−3868.

(43) Otero-de-la-Roza, A.; Johnson, E. R. Van der Waals interactions in solids using the exchange-hole dipole moment model. *J. Chem. Phys.* **2012**, *136*, No. 174109.

(44) Grimme, S.; Diedrich, C.; Korth, M. The Importance of Inter- and Intramolecular van der Waals Interactions in Organic Reactions: the Dimerization of Anthracene Revisited. *Angew. Chem., Int. Ed.* **2006**, *45*, 625−629.

(45) Řezáč, J.; Greenwell, C.; Beran, G. J. O. Accurate Noncovalent Interactions via Dispersion-Corrected Second-Order Møller−Plesset Perturbation Theory. *J. Chem. Theory Comput.* **2018**, *14*, 4711−4721.

(46) Greenwell, C.; Řezáč, J.; Beran, G. J. O. Spin-component-scaled and dispersion-corrected second-order Møller−Plesset perturbation theory: a path toward chemical accuracy. *Phys. Chem. Chem. Phys.* **2022**, *24*, 3695−3712.

(47) Beran, G. J. O. Solid state photodimerization of 9-tert-butyl anthracene ester produces an exceptionally metastable polymorph according to firstprinciples calculations. *CrystEngComm* **2019**, *21*, 758−764.

(48) Greenwell, C.; Beran, G. J. O. Inaccurate Conformational Energies Still Hinder Crystal Structure Prediction in Flexible Organic Molecules. *Cryst. Growth Des.* **2020**, *20*, 4875−4881.

(49) Smith, D. G. A.; Burns, L. A.; Simmonett, A. C.; Parrish, R. M.; Schieber, M. C.; Galvelis, R.; Kraus, P.; Kruse, H.; Di Remigio, R.; Alenaizan, A.; James, A. M.; Lehtola, S.; Misiewicz, J. P.; Scheurer, M.; Shaw, R. A.; Schriber, J. B.; Xie, Y.; Glick, Z. L.; Sirianni, D. A.; O'Brien, J. S.; Waldrop, J. M.; Kumar, A.; Hohenstein, E. G.; Pritchard, B. P.; Brooks, B. R.; Schaefer, H. F., 3rd; Sokolov, A. Y.; Patkowski, K.; DePrince, A. E., 3rd; Bozkaya, U.; King, R. A.; Evangelista, F. A.; Turney, J. M.; Crawford, T. D.; Sherrill, C. D. Psi4 1.4: Open-source software for high-throughput quantum chemistry. *J. Chem. Phys.* **2020**, *152* (18), No. 184108.

(50) Greenwell, C.; Beran, G. J. O. MP2D software library, 2018. https://github.com/Chandemonium/MP2D.

(51) Helgaker, T.; Klopper, W.; Koch, H.; Noga, J. Basis-set convergence of correlated calculations on water. *J. Chem. Phys.* **1997**, *106*, 9639−9646.

(52) Cook, C. J.; Li, W.; Lui, B. F.; Gately, Thomas J.; Al-Kaysi, R. O.; Mueller, L. J.; Bardeen, C. J.; Beran, G. J. O. A theoretical framework for the design of molecular crystal engines. *Chem. Sci.* **2023**, *14*, 937−949.

(53) Cook, C. J.; Perry, C. J.; Beran, G. J. O. Organic Crystal Packing Is Key to Determining the Photomechanical Response. *J. Phys. Chem. Lett.* **2023**, *14*, 6823−6831.

(54) Kitagawa, D.; Tomoda, R.; Ramos, S. A.; Beran, G. J. O.; Bardeen, C. J.; Kobatake, S. Distinctive Photomechanical Shape Change of p-Phenylenediacrylic Acid Dimethyl Ester Single Crystals Induced by a Spatially Heterogeneous Photoreaction. *Angew. Chem., Int. Ed.* **2025**, *64*, No. e202420243.

(55) Perry, C. J.; Beran, G. J. O. Investigating Cooperative Reactivity in Photomechanical Crystals Using First-Principles Density Functional Theory. *Cryst. Growth Des.* **2025**, *25*, 2561−2571.

(56) Bąkowicz, J.; Turowska-Tyrk, I. Structural Transformations in Crystals Induced by Radiation and Pressure. Part 10. The Crystallographic Picture of Photochemical Behaviour of bi(anthracene-9,10-dimethylene) under High Pressure. *Crystals* **2020**, *10*, 1031.

(57) Trzop, E.; Turowska-Tyrk, I. Monitoring structural transformations in crystals. 12. Course of an intramolecular [4 + 4] photocycloaddition in a crystal. *Acta Cryst. B* **2008**, *64*, 375−382.

(58) Gately, T. J.; Perry, C. J.; Weiss, S.; Lam, K.; Islam, I.; Almtiri, M. N.; Carta, V.; Beran, G. J. O.; Al-Kaysi, R. O.; Bardeen, C. J. Using Chemical Substitution to Engineer Photomechanical Cinnamalmalononitrile Crystals. *Cryst. Growth Des.* **2024**, *24*, 9544−9555.

(59) Bardeen, C. J. The Structure and Dynamics of Molecular Excitons. *Annu. Rev. Phys. Chem.* **2014**, *65*, 127−148.

(60) Shizuka, H.; Ishii, Y.; Hoshino, M.; Morita, T. Wavelength-dependent photochemical behavior in 9,10-dimethylenebianthracene. *J. Phys. Chem. A* **1976**, *80*, 30−32.

(61) Brancart, J.; Damme, J. V.; Prez, F. D.; Assche, G. V. Substituent effect on the thermophysical properties and thermal dissociation behaviour of 9-substituted anthracene derivatives. *Phys. Chem. Chem. Phys.* **2021**, *23*, 2252−2263.

(62) Jezowski, S. R.; Zhu, L.; Wang, Y.; Rice, A. P.; Scott, G. W.; Bardeen, C. J.; Chronister, E. L. Pressure Catalyzed Bond Dissociation in an Anthracene Cyclophane Photodimer. *J. Am. Chem. Soc.* **2012**, *134*, 7459−7466.

(63) Han, M. H. Non-linear Arrhenius plots in temperature-dependent kinetic studies of enzyme reactions: I. Single transition processes. *J. Theor. Biol.* **1972**, *35*, 543−568.

(64) Silvius, J. R.; McElhaney, R. N. Non-linear arrhenius plots and the analysis of reaction and motional rates in biological membranes. *J. Theor. Biol.* **1981**, *88*, 135−152.

(65) Berges, A. J.; Li, W.; Xu, W.; Tong, F.; Al-Kaysi, R. O.; Hayward, R. C.; Bardeen, C. J. Photomechanical Structures Based on Porous Alumina Templates Filled with 9-Methylanthracene Nanowires. *Crystals* **2022**, *12*, 808.

(66) Xu, W.; Sanchez, D. M.; Raucci, U.; Zhou, H.; Dong, X.; Hu, M.; Bardeen, C. J.; Martinez, T. J.; Hayward, R. C. Photo-actuators via epitaxial growth of microcrystal arrays in polymer membranes. *Nat. Mater.* **2023**, *22*, 1152−1159.

(67) Halabi, J. M.; Ahmed, E.; Sofela, S.; Naumov, P. Performance of molecular crystals in conversion of light to mechanical work. *Proc. Nat. Acad. Sci. U.S.A.* **2021**, *118*, No. e2020604118.

(68) Guo, T.; Zheng, X.; Palffy-Muhoray, P. Impedance matching in an elastic actuator. *Soft Matter* **2021**, *17*, 4191−4194.

(69) Dong, X.; Guo, T.; Kitagawa, D.; Kobatake, S.; Palffy-Muhoray, P.; Bardeen, C. J. Effects of Template and Molecular Nanostructure on the Performance of Organic-Inorganic Photomechanical Actuator Membranes. *Adv. Funct. Mater.* **2020**, *30*, No. 1902396.

(70) Dong, X.; Guo, T.; Kitagawa, D.; Kobatake, S.; Palffy-Muhoray, P.; Bardeen, C. J. Performance of Composite Glass−Diarylethene Crystal Photomechanical Actuator Membranes. *ACS Appl. Mater. Interfaces* **2022**, *14*, 27149−27156.